CONF-960172--1

Coincidences between light particles, evaporation residues, and complex fragments emitted in the reaction $^{58}Ni + ^{58}Ni$ at 500 MeV bombarding energy

J. Gomez del Campo, D. Shapira
Oak Ridge National Laboratory, Oak Ridge, TN, USA

E. Chavez, M. E. Ortiz, and A. Dacal
IFUNAM, Mexico

A. D'Onofrio
Universitá degli Studi de Salerno, Salerno, Italy

F. Terrasi
Seconda Universitá di Napoli, Naples, Italy.

ABSTRACT

Light particles (protons and alphas) were measured in coincidence with complex fragments ($4 < Z < 10$) and evaporation residues ($Z > 40$) using the large detector array HILI. A ^{58}Ni beam of 500 MeV extracted from the HHIRF tandem accelerator was used to bombard a ^{58}Ni target of 99% enrichment. A good account of the proton and alpha spectra in coincidences with the residues can be achieved only by including in the statistical model calculation the emission of complex fragments and allowing a small emission of a dinuclear configuration formed prior to fusion. The relative kinetic energy spectra between the complex fragments and the residues show a typical Coulomb peak consistent with emission from the compound nucleus and the out of plane angular correlation shows that the emission is coplanar.

I. INTRODUCTION

Large multidetector systems recently developed [1,2,3] for the study of heavy-ion collisions at bombarding energies below 100 MeV/nucleon have produced a large body of valuable data particularly for central collisions. Detailed studies of particle-particle correlations [4,5] have produced new information about the lifetime and size of the collision zone. Detailed studies of complex fragments ($Z > 2$) [2] provide important information about the competition between multifragmentation and sequential emission processes. Even for energies below 15 MeV/nucleon (6) fusion and incomplete fusion studies with large detector arrays can give valuable and surprising data. In the study of $^{79}Br + ^{27}Al$ [6] it was shown that the α-particles studied in coincidence with evaporation residues (ER) are emitted with extremely low barriers indicating that the emission occurs from a highly deformed compound nucleus or from a dinuclear system formed prior to fusion. Also in the same study it was shown that the measured cross section for emission of deuterons and tritons are much smaller than predicted by statistical models. To increase our understanding of many of these effects, in this work we present data on a symmetric system $^{58}Ni + ^{58}Ni$ measured with the large detector array HILI (1) at a bombarding energy of 500 MeV. We present data on the proton α and complex fragment ($Z > 4$) spectra measured in coincidence with evaporation residues.

II. EXPERIMENTAL TECHNIQUES

Light particles (p and α) emitted from collisions of $^{58}Ni + ^{58}Ni$ at 500 MeV bombarding energy were measured in coincidence with complex fragments ($4 < Z < 10$) and evaporation residues ($Z > 40$) using the large detector array HILI [1]. The ^{58}Ni beam was extracted from the Tandem accelerator of the HHIRF at ORNL. Self supported ^{58}Ni foils of 200 $\mu g/cm^2$ were prepared by evaporation of ^{58}Ni powder enriched to 99%. The target thickness was determined by α-particle ranging. The HILI (Heavy Ion Light Ion) detector is a large acceptance, multidetector system which is capable of detecting heavy ions in coincidence with light ions. It consists of three major detector subsystems (1) a four quadrant parallel plate detector (PPAC) with a plane of position sensing wires; (2) a four-quadrant gas-ionization chamber (IC); and (3) two 96 element hodoscopes of plastic scintillator "phoswich" telescopes. Except for a 2° beam hole in the center, the detector spans an opening angle of 20° horizontally and 16° vertically. An exploded view of the detector is shown in Fig. 1. For the present experiment, an additional slit covering the detector up to 5° was placed in front of the PPAC to avoid the very intense counting rate due to the elastic scattering of ^{58}Ni on ^{58}Ni.

Coincident light particles were detected with the hodoscope array of the HILI system which is composed of 192 plastic scintillators that were calibrated with recoil protons produced by an ^{16}O beam on a polypropylene target. The calibration for particles of higher Z and M was done as described in Ref. 1. Additional checks were carried out by comparing the α-particle and p spectra obtained with the hodoscope to those obtained from calibrated Si detector telescopes. For example, the energies measured by hodoscope elements agreed with energies of Si telescopes within 2 MeV for the case of singles α spectra measured for the $^{58}Ni + ^{58}Ni$ reaction at 500 MeV bombarding energy. We estimate the absolute energy calibration to be better than 3%. A typical example of two dimensional E-ΔE measured spectrum used for Z-identification is shown in Fig. 2. The horizontal axis shows the total E signal of the hodoscope element and the vertical axis shows the ΔE signal extracted from the 0.5 mm plastic detector placed in front of each hodoscope. The p's and α particles are clearly indicated in the figure. The rest of the events are the neutrals (n and γ's), and fragments that stop in the ΔE.

The complex fragments ($4 < Z < 10$) also called IMF's (intermediate mass fragments) usually have energies high enough and cannot be stopped in the ionization chamber (IC), and therefore, the best identification is achieved by measuring the energy loss in the IC and the total energy in the hodoscopes. In Fig. 3 a display of the ΔE(IC) vs. E (hodoscopes) is shown and the fragments of C, N and O are clearly identified.

The evaporation residues were measured with the ionization chambers (IC) of the HILI system which were calibrated using the elastic scattering of $^{58}Ni + ^{58}Ni$. The calibration was extended to lower energies using fragments of Z lower than the beam that penetrated through the IC and whose maximum energy loss can be determined by using stopping power tables. The major uncertainty on the energy calibration comes from the energy loss corrections that are needed because the fragments lose energy in the entrance parallel plate detector and the foils to the IC. For the present measurement an overall absolute energy calibration was estimated to be about 3%. In Fig. 4 a two dimensional plot of the ΔE(IC) vs. E(IC) for one of the four quadrants of the HILI detector is presented. In that figure, the location of the ^{58}Ni is indicated as well as that of the ER. Between the

ER and the beam are several well resolved groups all belonging to fragments of Z(~ 20) close to the beam . The ER cannot be resolved by individual Z (all around 50) primarily due to the low energy per nucleon (~ 2 MeV) with which they are produced in the reaction. (This makes the fragments to lie below the Bragg peak on the stopping power curves relevant to the foils and gas used in the IC.)

III. RESULTS AND ANALYSIS

From the two dimensional spectrum such as that shown in Fig. 2 the energy spectra of the light particles is extracted by projecting each particle group into the energy axis (horizontal). The data shown in Fig. 2 corresponds to one hodoscope element (from the 192 of the HILI system) and one scattering angle (10°). An analysis of each individual spectrum of the 192 elements will be tedious and repetitive, so we have chosen instead to sum the spectra over the angular coverage (5° to 25°) of the detector system. The resulting spectra for protons is shown in Fig. 5 (open circles). Two constraints have been imposed on these spectra, the first one is that the p's are in coincidence with the ER gate shown in Fig. 4 and the second is on charged particle (p or α) multiplicity m. Thus, the panel on the bottom shows the p energy spectra when one or more charged particles (at least one p) are identified in any of the hodoscopes detectors; the middle panel on Fig. 5 corresponds to $m \geq 2$ (again at least one p) and the top panel for $m \geq 3$. The vertical scale given in the figure corresponds to the differential multiplicity dm/dE defined as the number of p's in a given energy interval dE divided by the total number of ER's registered in the IC part of HILI (see Fig. 4). In a similar procedure the α-particle spectra were extracted with the same constraints as those of the p's and they are shown in Fig. 6.

The crosses plotted in Figs. 5 and 6 (labeled CF) represent the statistical model calculations assuming a complete fusion reaction and equilibrium decay. The calculations are of the Monte Carlo type and were done with the code LILITA [7]. The same geometrical constraints imposed on the data by the HILI detector were employed in the calculations. The relevant statistical model parameters employed in the calculations were the level density parameter a = A/10, the critical angular momentum for fusion 68($\hbar$), and optical model transmission coefficients extracted from the parameters of Ref. 8. In addition the calculations were carried out using only light particle decay channels of n, p, α, d , and t. From the comparisons shown in Figs. 5 and 6, the first interesting observation is that the predicted differential multiplicity disagrees with the experimental one with increasing total charged particle multiplicity m, i.e., is a few percent off for $m \geq 1$ and about a factor of four for $m \geq 3$. Also, a slight shift on the maximum of the calculated spectra for both p and α's is evident. On the other hand, the slope of the high energy part of the spectra is remarkably well reproduced by the calculations indicating that the use of A/10 for a is an adequate choice (essentially, the slope depends mostly on the a parameter and the excitation energy (Ex) of compound system, i.e., on the temperature t since $Ex = a\ t^2$). Several factors can influence the statistical model calculations, and the first and most obvious one is that not only light particle channels are important. In particular, for the $^{58}Ni + ^{58}Ni$ reaction studied at 11 MeV/nucleon [9], it was shown that the emission cross section of complex fragments can be high, and account for as much as 20% of the fusion cross section. Also, in the present experiment sizable amounts of complex fragments are seen (see Fig. 3). To incorporate the decay of heavier fragments, it was necessary to compute the cross section for emission of many channels in a first chance and later couple that decay to a multistep emission process. For the present experiment, this was done using the code BUSCO [9] with as many as 400 channels (up to Ca) for the first chance emission and the

output of this code coupled to LILITA (with only light particle channels) for the remaining of the decay chain. Results of this approach are shown in Figs. 7 (for p's) and 8 (for α's) and are represented by the crosses (labeled CF + IMF). The results of this calculation are in much better agreement with the experiment than for the case of light particle emission only (Figs. 5 and 6) and even for the $m \geq 3$ the discrepancy now is smaller than a factor of two. Clearly, what these comparisons show is that the inclusion of IMF's is very important in order to understand the compound nucleus deexcitation process.

Another perspective on the importance of incorporating IMF's on the deexcitation process can be obtained by studying the total yields of p's and α's as a function of the multiplicity m. The bar diagrams shown in Figs. 9 and 10 show the yield of p's (Fig 9) and α's(Fig 10) integrated over the particle energy. The vertical axis shows the number of p's or α's divided by the total number of ER's detected. The horizontal axis gives the charged particle multiplicity m already discussed in connection with Figs 5-8. The calculated histograms labeled CF correspond to a complete fusion and equilibrium decay process, without the IMF channels and those labeled CF + IMF correspond to the case were the IMF decays are included. As can be seen from the comparisons shown in Figs. 9 and 10, the overall experimental multiplicities are much better reproduced by the CF + IMF calculations.

In addition to the light particle measurements just discussed, data on ER's and IMF's are also available. Figures 3 and 4 show the relevant two dimensional plots. The experimental quantities measured for the IMF's were: Z, E and the direction of emission with respect to the beam axis defined by the polar angle Θ and azimuthal angle Φ. For the ER's, only the E and direction of emission were determined and not the Z, however this can be estimated from the Monte Carlo calculations. An interesting quantity that could be helpful in the analysis of the emission of the IMF's is the relative kinetic energy ε_{rel} of the coincident pair, ER and IMF. It is defined by $\varepsilon_{rel} = 1/2\ \mu\ |\mathbf{V}_{IMF}-\mathbf{V}_{ER}|^2$, where μ is the reduced mass of the pair, $\mathbf{V}_{IMF}$ is the lab velocity vector for the emitted IMF, and $\mathbf{V}_{ER}$ is that of the ER. The experimental results for the relative kinetic energy are shown in Fig. 11 (open circles) for the case of Z = 6 (C) in coincidence with the ER's. The vertical scale has the same meaning as that of Figs 5-8. The crosses plotted in Fig. 11 correspond to the statistical emission process for the IMF and they are part of the same calculations labeled CF + IMF in Figs. 7 and 8. It is interesting to note that the maximum of the spectrum shown in Fig. 11 occurs at about 50 MeV, a value close to the Coulomb barrier of C emitted from the compound nucleus ^{116}Ba. Another important consequence of the compound nucleus emission mechanism for the IMF is that they are emitted mostly in the first step of the reaction when the angular momentum of the compound nucleus is the highest. This implies that the IMF and ER lay on the same reaction plane, i.e., the difference of their respective azimuthal angle Φ should be 180° regardless of the polar angle Θ. Therefore, a construction of the angular correlation $\Delta\Phi = |\Phi_{ER}-\Phi_{IMF}|$ which will reflect the degree of coplanarity of the emission process will be extremely useful. On Fig. 12 such an angular correlation is presented where the circles are the experimental data and the crosses are the calculations. The most important conclusion to be drawn from the comparisons of Fig. 12 is that clearly the emission is highly coplanar (maximum at $\Delta\Phi = 180°$). Details on the width and skewness of the $\Delta\Phi$ distribution depend more on the detector response than on the emission process.

Finally, a comment on the possible source of discrepancies seen in the maxima of the p and α spectra (see Figs. 5-8) should be made. In the $^{79}Br + ^{27}Al$ reaction studied previously [6] the shift on the maxima of the α spectra between the CF calculations and the data was about 10 MeV, certainly much larger than observed in Figs. 6 or 8. These shifts were explained by emissions from a dinuclear system formed prior to fusion. In the model given in Ref. 6, the dinuclear mechanism explains very well the data, and it is noted that the most important parameters are the maximum angular momentum for fusion J_c and for formation of the dinuclear system J_g where $J_g > J_c$. For the present reaction $^{58}Ni + ^{58}Ni$, we have used the same dinuclear model with the values of $J_c = 60(\hbar)$ and $J_g = 75\ (\hbar)$. Below an entrance channel angular momentum of 60 ($\hbar$) only complete fusion is considered. A summary of the three different calculations discussed in this work for the energy spectra of protons and α 's (in coincidence with ER's) is given in Figs. 13 and 14, respectively. The coincidence requirement is $m \geq 1$ and the calculations labeled CF and CF + IMF have been discussed earlier in connection with Figs. 7 and 8. The top panels on Fig. 13 and 14 show the comparisons between the experiment and calculations (labeled DN) which correspond to the emission from the dinuclear system. As can be seen from the figures, a clear improvement in the location of the maxima of the p and α spectra is evident and corroborates the mechanism presented for the $^{79}Br + ^{27}Al$ reaction (6).

IV. CONCLUSIONS

From the comparison between experiment and calculations shown in Figs. 5-12, it is clear that the overall emission process in $^{58}Ni + ^{58}Ni$ at 500 MeV is consistent with complete fusion and equilibrium decay. In particular ,by studying the light particle multiplicities it is concluded that it is necessary to include the IMF channels in the deexcitation process. Also, this conclusion is supported by studying directly the IMF's emitted in coincidence with ER. The spectra of p's and α's (Figs. 5-8) compared to the calculations show small discrepancies at low energies and on the location of the maxima. This shift is indicative of deformation of the compound nucleus or of emission from a dinuclear system formed prior to fusion.

ACKNOWLEDGMENTS

Oak Ridge National Laboratory is managed by Lockheed Martin Energy Systems, Inc. under contract DE-AC05-840R21400 with the U.S. Department of Energy. This work was also supported in part by NATO grant CR6.890807d and by CONACYT (Mexico) contract # 1103-E9102.

References

1. D. Shapira *et al.*, Nucl. Inst. Methods, Phys. Res. A301, 76 (1991).
2. R. T. de Souza *et al.*, Nucl. Inst. Methods, Phys. Res. A295, 109 (1990).
3. E. Plagnol *et al.*, Rev. Mex. Fisica, **40** ,175(1994).
4. T. Glasmacher *et al.*, Phys. Rev C51, 3489 (1995).
5. M. Korolija, *et al.*, Phys. Rev. Lett. **67**, 57 (1991).
6. J. Gomez del Campo, *et al.*, Phys. Rev. C, to be published.
7. J. Gomez del Campo and R. G. Stokstad, ORNL/TM-7295 (1981).
8. C. M. Perey and F. G. Perey , Atom. Data and Nucl. Data Tables **17**, 1 (1976).
9. J. Gomez del Campo *et al.*, Phys. Rev. Lett. **61**, 290 (1988).

FIGURE CAPTIONS

Fig. 1. An exploded view of the HILI detector.

Fig. 2. ΔE vs. E array for the light particles emitted in the reaction $^{58}Ni + ^{58}Ni$ at $E(^{58}Ni) = 500$ MeV. The proton and α groups can be clearly seen. The light particles are detected by the plastic elements of the hodoscopes of the HILI system.

Fig. 3. ΔE vs. E array for intermediate mass fragments (IMF's) emitted in collisions of $^{58}Ni + ^{58}Ni$ at $E(^{58}Ni) = 500$ MeV. The array is constructed by plotting the energy of the fragments deposited in the ionization chamber, against the energy deposited in the hodoscope detector. This plot corresponds to one of the four quadrants covered by the HILI system.

Fig. 4. ΔE vs. E array for heavy fragments stopped in the ionization chamber of HILI. The elastic beam ^{58}Ni and the evaporation residues(ER) of the compound nucleus formed in the $^{58}Ni + ^{58}Ni$ fusion reaction are clearly indicated in the figure.

Fig. 5. Experimental energy spectra of p (circles) emitted in coincidence with ER's of the $^{58}Ni + ^{58}Ni$ at 500 MeV bombarding energy. The three panels correspond to different charged particle (p or α) multiplicity (m) conditions. The crosses (CF) are the results of Monte Carlo statistical model calculations assuming complete fusion and equilibrium decay using only the n, p, α, d, and t decay channels.

Fig. 6. Experimental energy spectra of α (circles) emitted in coincidence with ER's of the $^{58}Ni + ^{58}Ni$ at 500 MeV bombarding energy. The three panels correspond to different charged particle (p or α) multiplicity (m) conditions. The crosses (CF) are the results of Monte Carlo statistical model calculations assuming complete fusion and equilibrium decay using only the n, p, α, d, and t decay channels.

Fig. 7. Experimental energy spectra of p (circles) emitted in coincidence with ER's of the $^{58}Ni + ^{58}Ni$ at 500 MeV bombarding energy. The three panels correspond to different charged particle (p or α) multiplicity (m) conditions. The crosses(CF + IMF) are the results of Monte Carlo statistical model calculations assuming complete fusion and equilibrium decay using IMF decay channels (up to Ca) in addition to the light particle (n, p, α, d, and t) channels.

Fig. 8. Experimental energy spectra of α (circles) emitted in coincidence with ER's of the $^{58}Ni + ^{58}Ni$ at 500 MeV bombarding energy. The three panels correspond to different charged particle (p or α) multiplicity (m) conditions. The crosses(CF + IMF) are the results of Monte Carlo statistical model calculations assuming complete fusion and equilibrium decay using IMF decay channels (up to Ca) in addition to the light particle (n, p, α, d, and t) channels.

Fig. 9. Multiplicity distribution of p's in coincidence with ER for the $^{58}Ni + ^{58}Ni$ reaction. These distributions were obtained by integrating over energy the spectra shown in Figs. 5-7. The calculated histograms (CF and CF + IMF) corresponds to the statistical model calculations presented in Figs. 5-7.

Fig. 10. Multiplicity distribution of α's in coincidence with ER for the $^{58}Ni + ^{58}Ni$ reaction. These distributions were obtained by integrating over energy the spectra shown in Figs. 6-8. The calculated histograms (CF and CF + IMF) corresponds to the statistical model calculations presented in Figs. 6 and 8.

Fig. 11. Experimental(circles) relative kinetic energy spectra (ε_{rel}) for the correlation of carbon ions and ER's emitted in the fusion of $^{58}Ni + ^{58}Ni$. The crosses are the results of the complete fusion calculation and equilibrium decay including IMF channels in addition to the light particle channels.

Fig. 12. Out of plane angular correlation $\Delta\Phi$ defined by the difference of azimuthal laboratory angles (Φ) for the IMF and ER. The circles are the experimental values.

Fig. 13. Experimental energy spectra of p (circles) emitted in coincidence with ER's of the $^{58}Ni + ^{58}Ni$ at 500 MeV bombarding energy. The three panels correspond to the same experimental data for $m \geq 1$ but different calculations. The calculations labeled CF and CF + IMF are discussed in relation to Figs. 5 and 7 and the one labeled DN corresponds to a dinuclear emission prior to fusion.

Fig. 14. Fig. 13. Experimental energy spectra of α (circles) emitted in coincidence with ER's of the $^{58}Ni + ^{58}Ni$ at 500 MeV bombarding energy. The three panels correspond to the same experimental data for $m \geq 1$ but different calculations. The calculations labeled CF and CF + IMF are discussed in relation to Figs. 6 and 8 and the one labeled DN corresponds to a dinuclear emission prior to fusion.

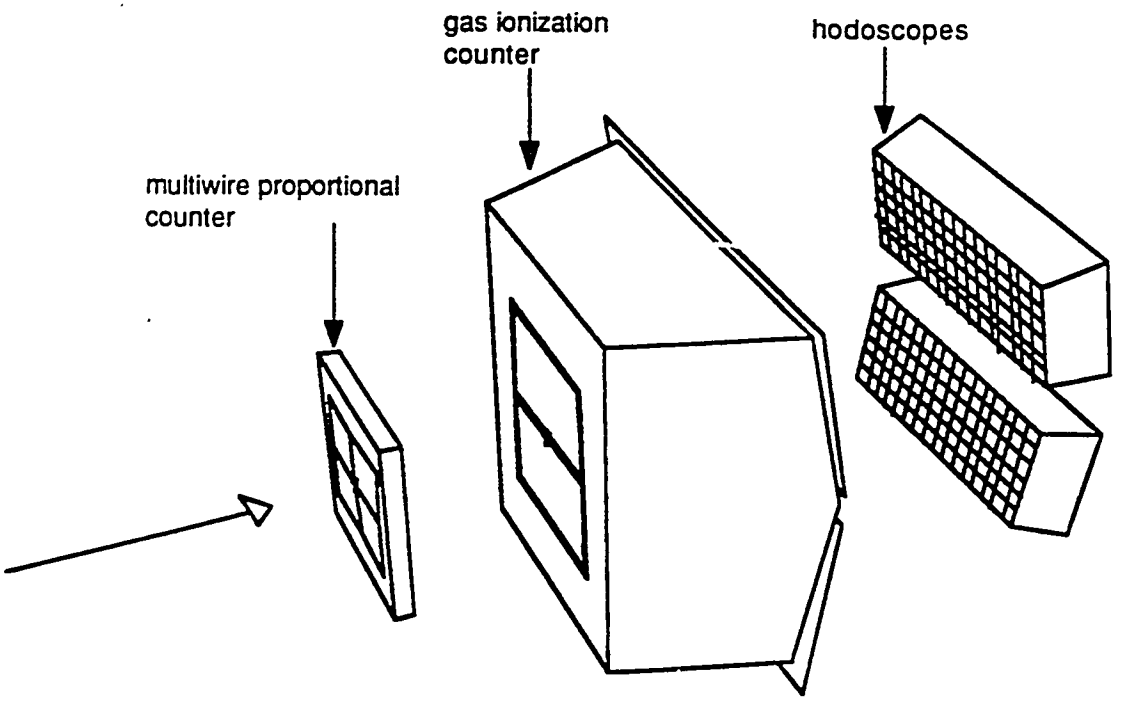
gas ionization
counter
hodoscopes
multiwire proportional
counter

Fig 1

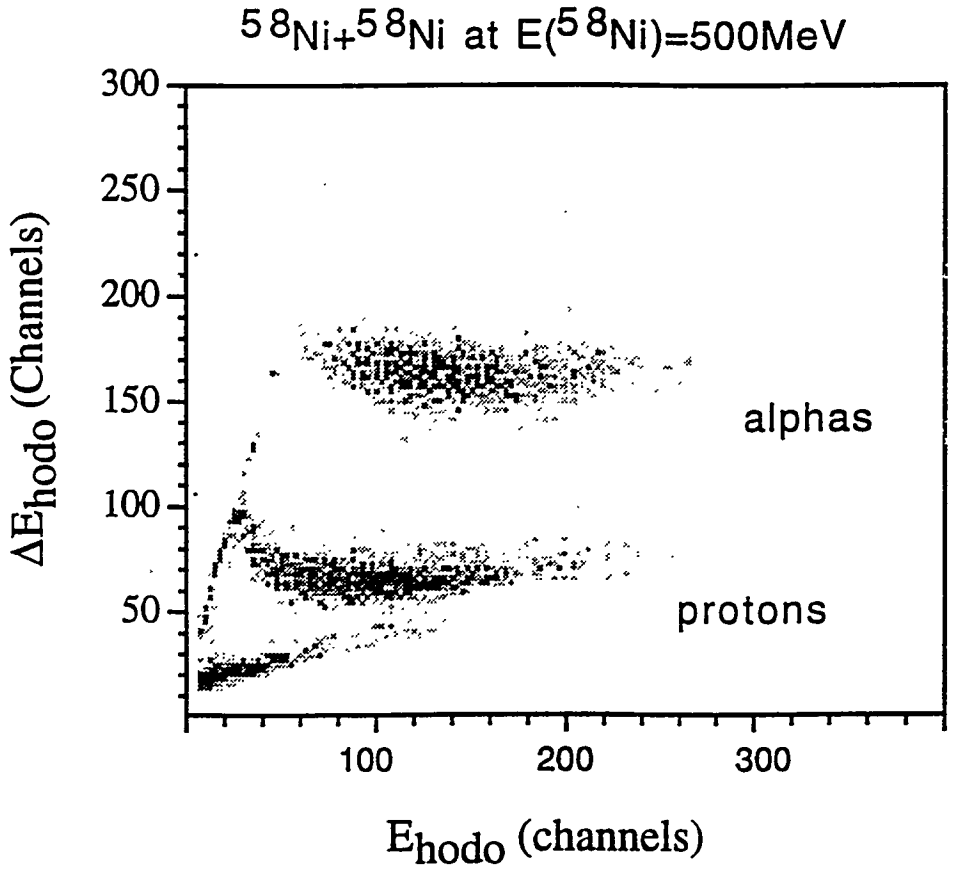
58Ni+58Ni at E(58Ni)=500MeV
300
250
200
150
100
50
ΔEhodo (Channels)
alphas
protons
100
200
300
Ehodo (channels)

Fig 2

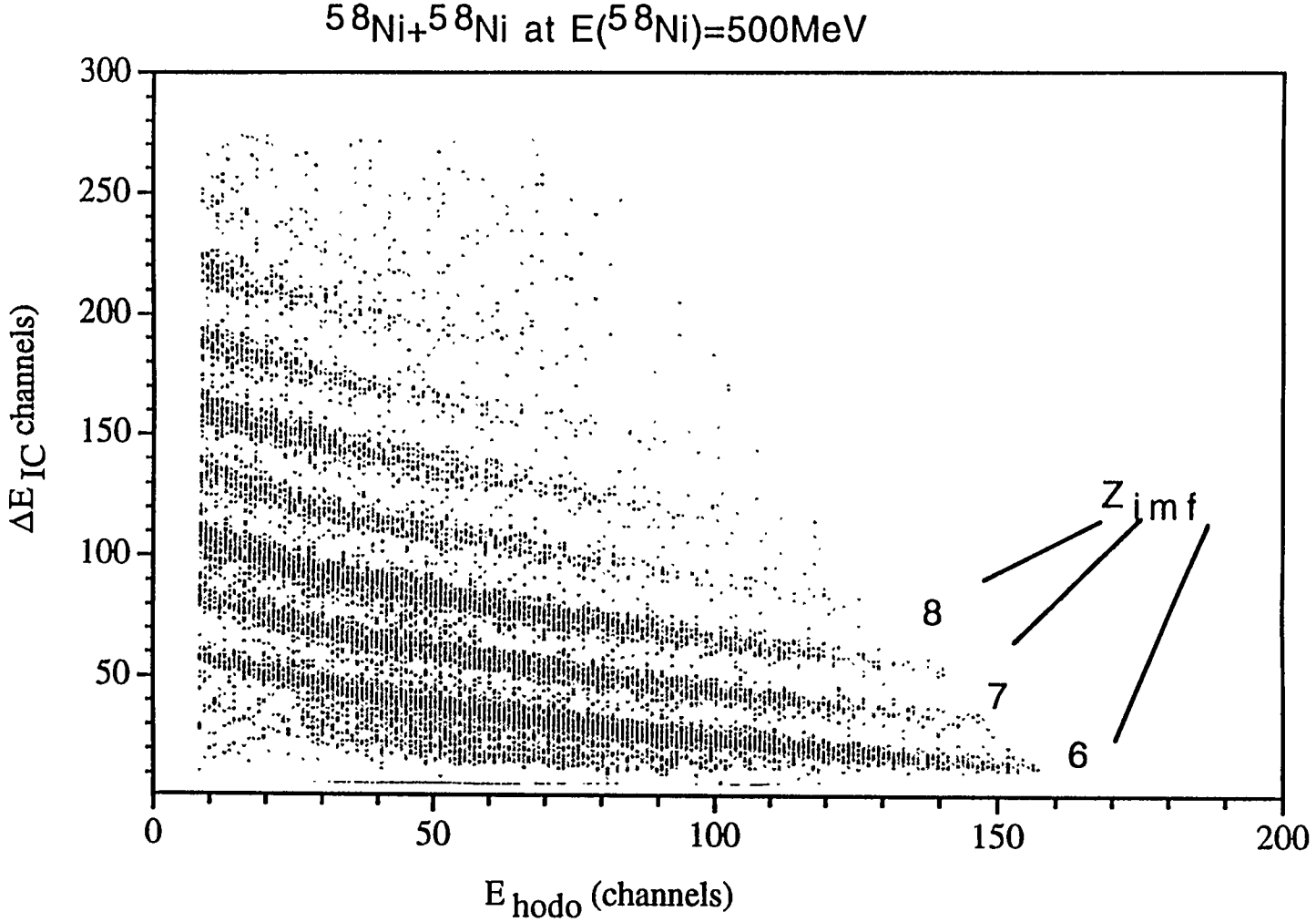
58Ni+58Ni at E(58Ni)=500MeV
ΔE IC channels)
E hodo (channels)
Z imf
8
7
6
300
250
200
150
100
50
0
50
100
150
200

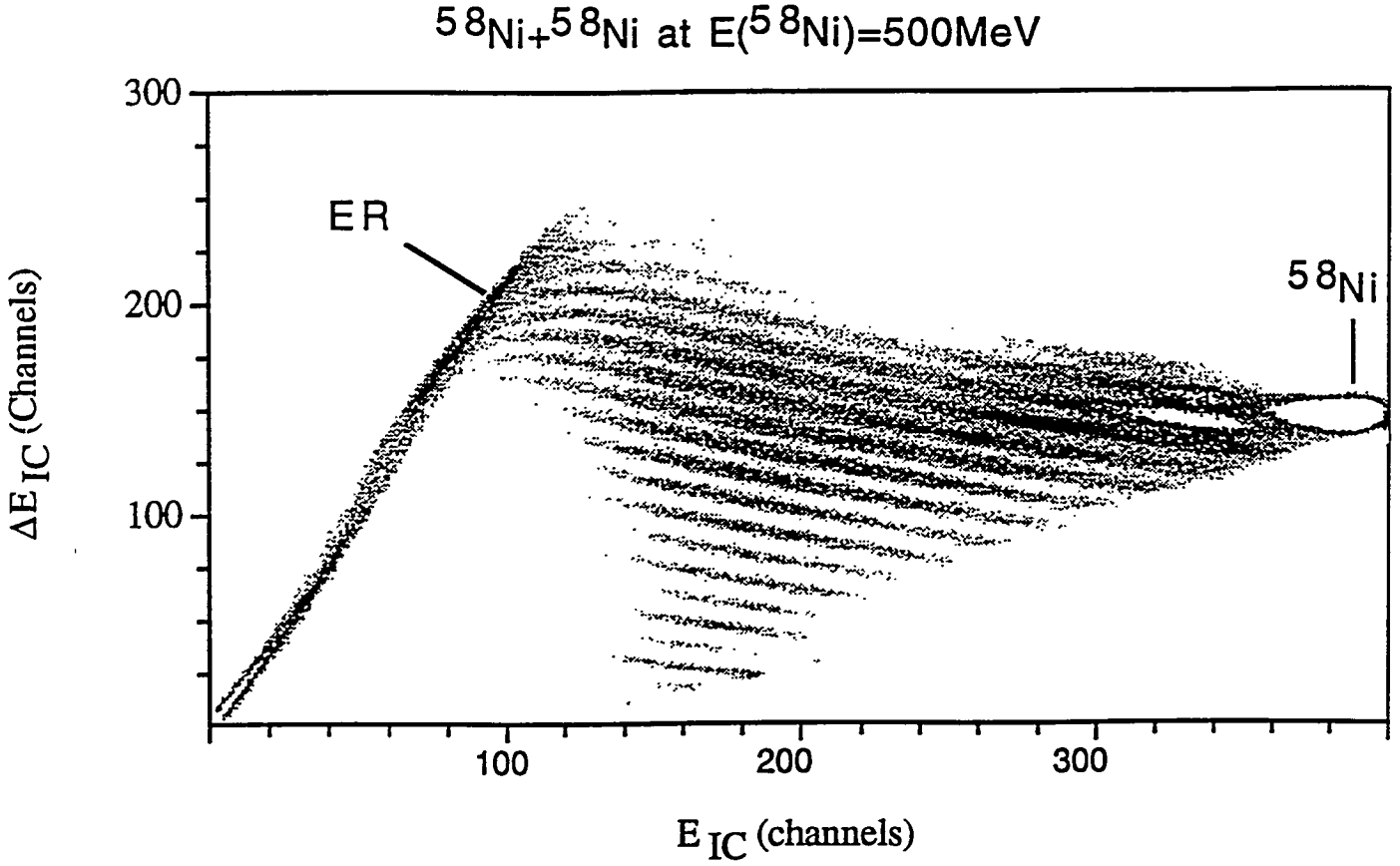
$^{58}Ni+^{58}Ni$ at E(^{58}Ni)=500MeV
ER
^{58}Ni
300
200
100
100
200
300
ΔE_{IC} (Channels)
E_{IC} (channels)

fig 4

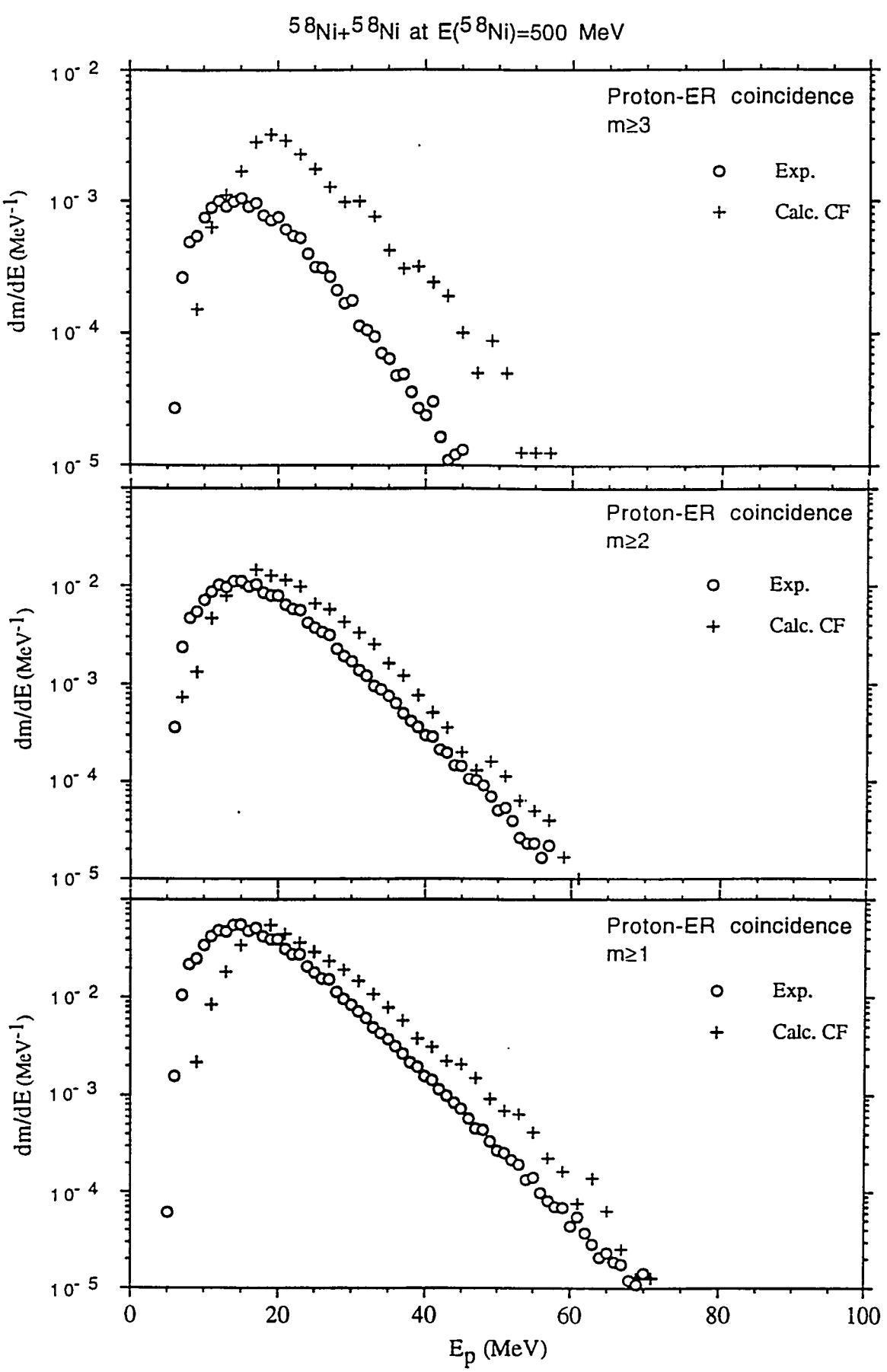
58Ni+58Ni at E(58Ni)=500 MeV
Proton-ER coincidence
m≥3
Exp.
Calc. CF
Proton-ER coincidence
m≥2
Exp.
Calc. CF
Proton-ER coincidence
m≥1
Exp.
Calc. CF
dm/dE (MeV-1)
10- 2
10- 3
10- 4
10- 5
0
20
40
60
80
100
Ep (MeV)

Fig 5

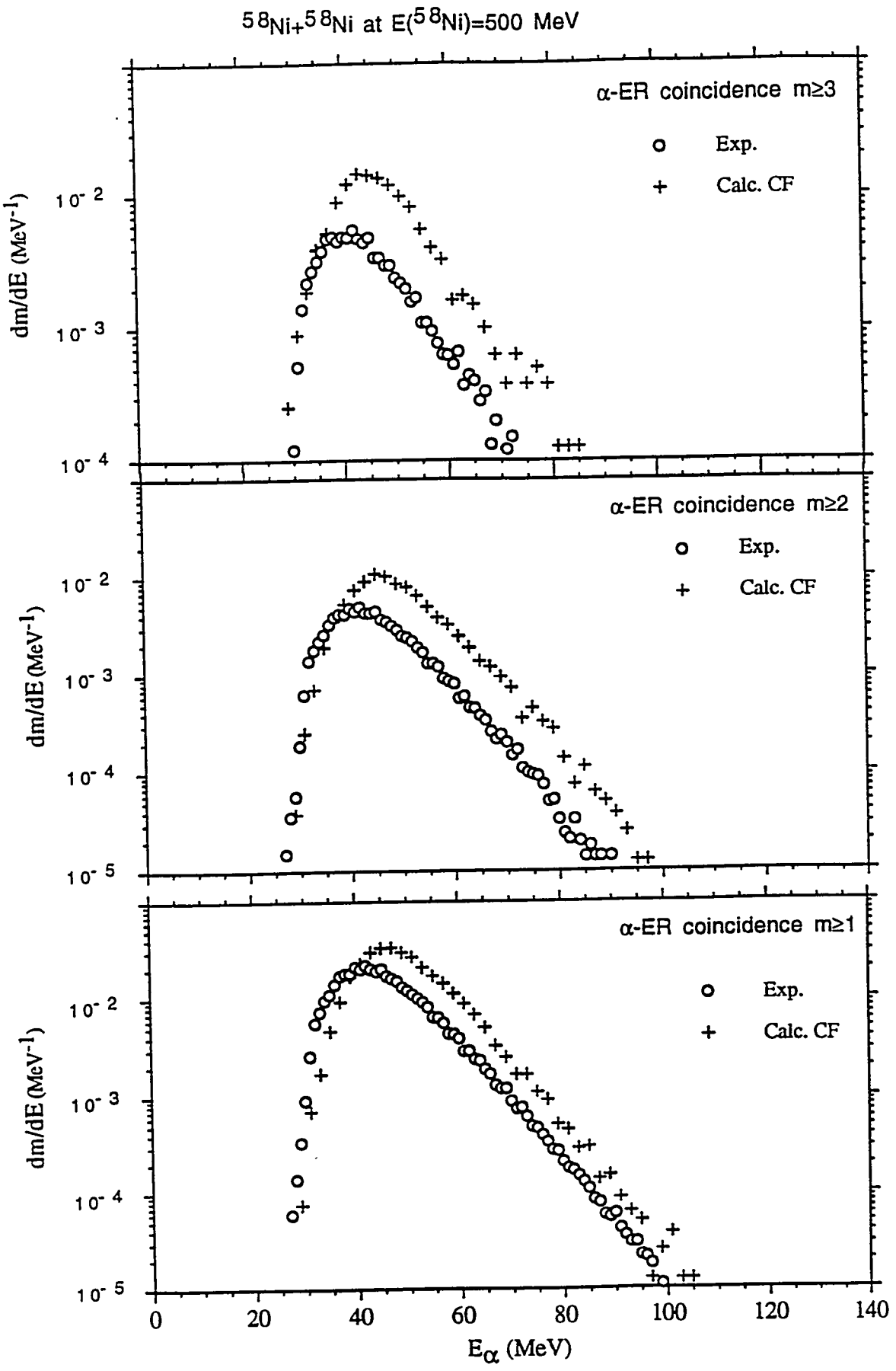
$^{58}Ni+^{58}Ni$ at E(^{58}Ni)=500 MeV
α-ER coincidence m≥3
Exp.
Calc. CF
α-ER coincidence m≥2
Exp.
Calc. CF
α-ER coincidence m≥1
Exp.
Calc. CF
dm/dE (MeV^{-1})
10^{-2}
10^{-3}
10^{-4}
10^{-5}
0
20
40
60
80
100
120
140
E_α (MeV)

Fig 6

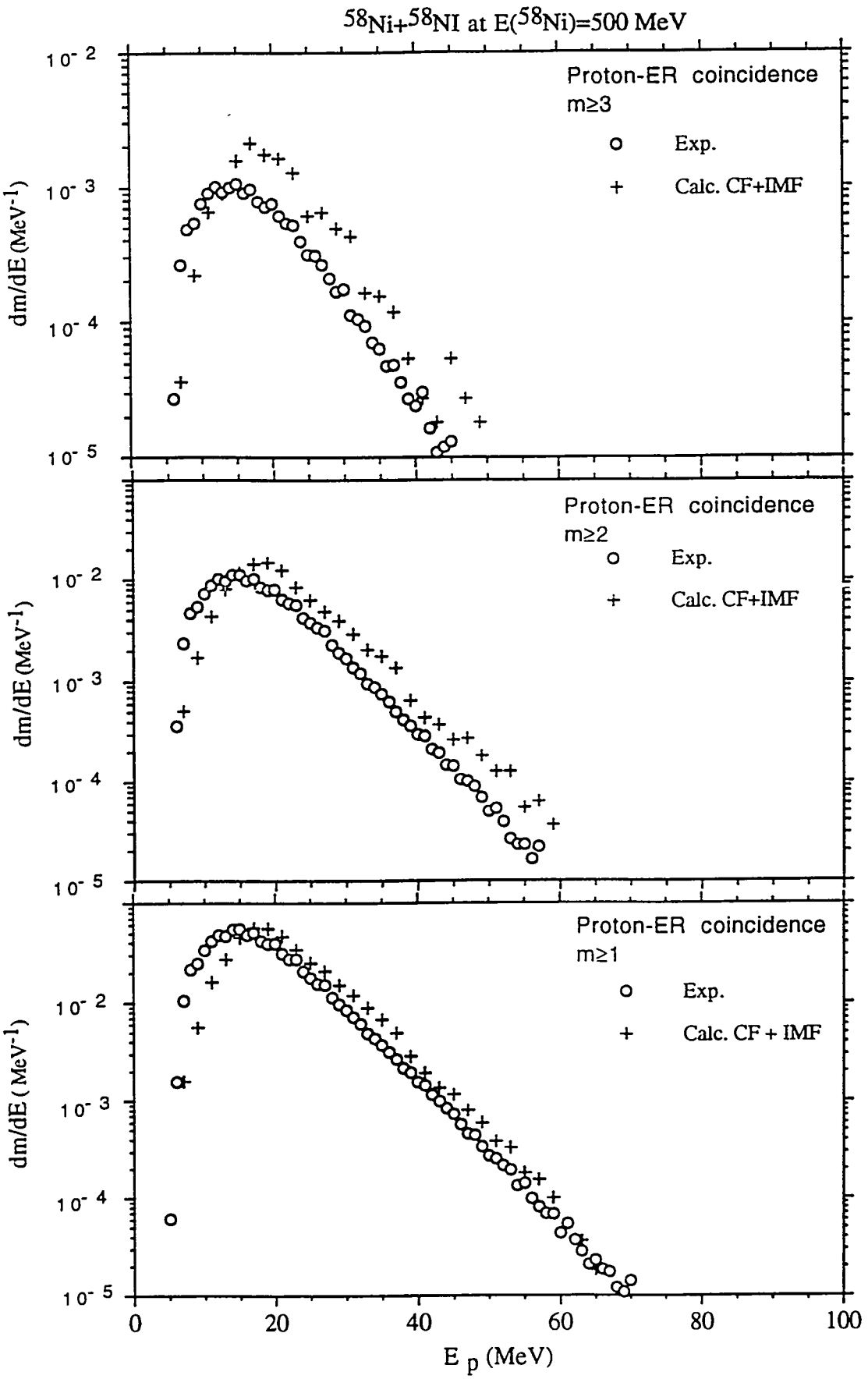
58Ni+58NI at E(58Ni)=500 MeV
Proton-ER coincidence
m≥3
Exp.
Calc. CF+IMF
Proton-ER coincidence
m≥2
Exp.
Calc. CF+IMF
Proton-ER coincidence
m≥1
Exp.
Calc. CF + IMF
dm/dE (MeV-1)
dm/dE (MeV-1)
dm/dE (MeV-1)
10- 2
10- 3
10- 4
10- 5
0
20
40
60
80
100
E p (MeV)

Fig 7

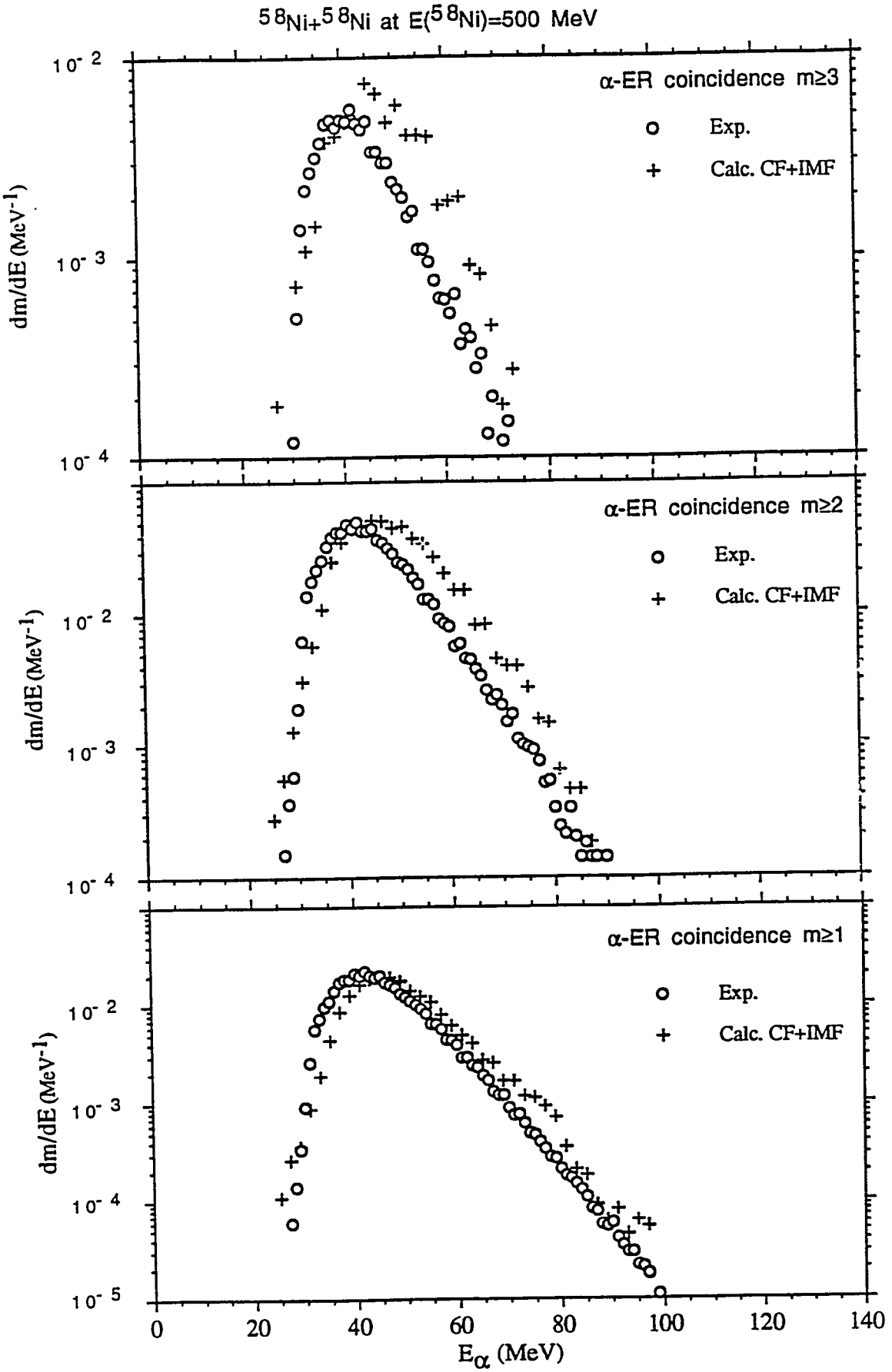
$^{58}Ni+^{58}Ni$ at E(^{58}Ni)=500 MeV
α-ER coincidence m≥3
Exp.
Calc. CF+IMF
α-ER coincidence m≥2
Exp.
Calc. CF+IMF
α-ER coincidence m≥1
Exp.
Calc. CF+IMF
dm/dE (MeV^{-1})
10^{-2}
10^{-3}
10^{-4}
10^{-5}
0
20
40
60
80
100
120
140
E_α (MeV)

Fig 8

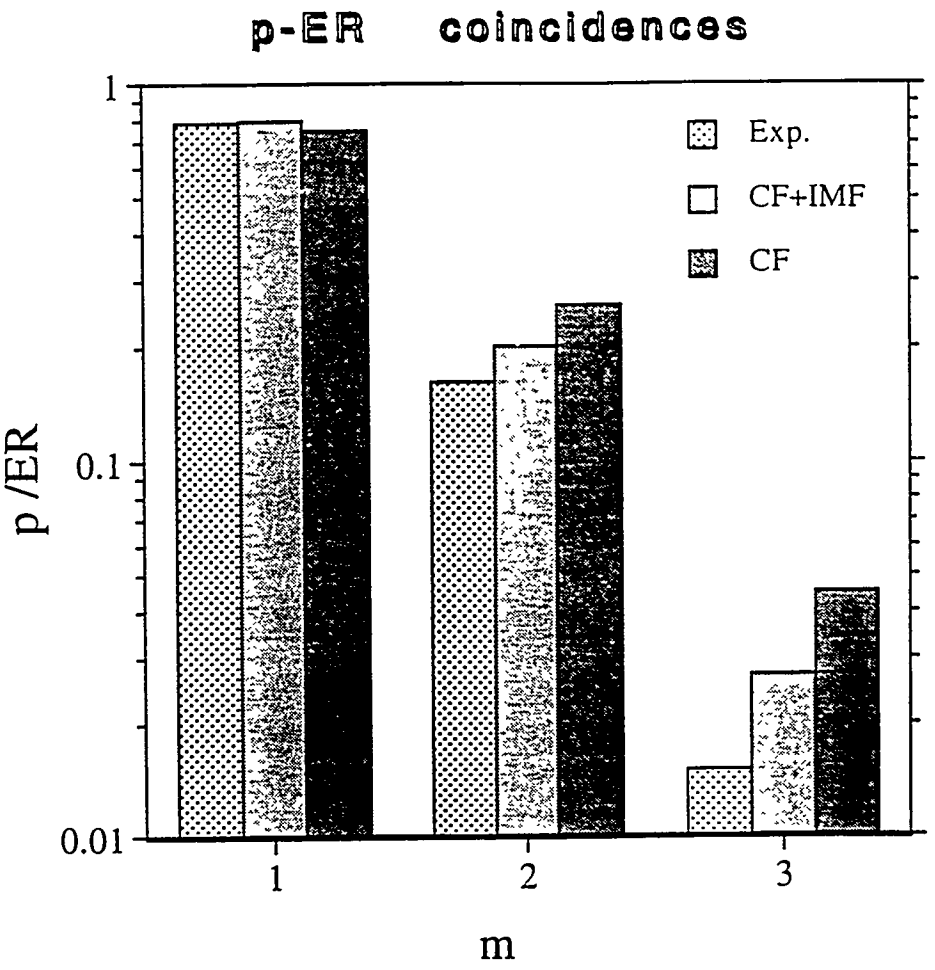

Fig 9

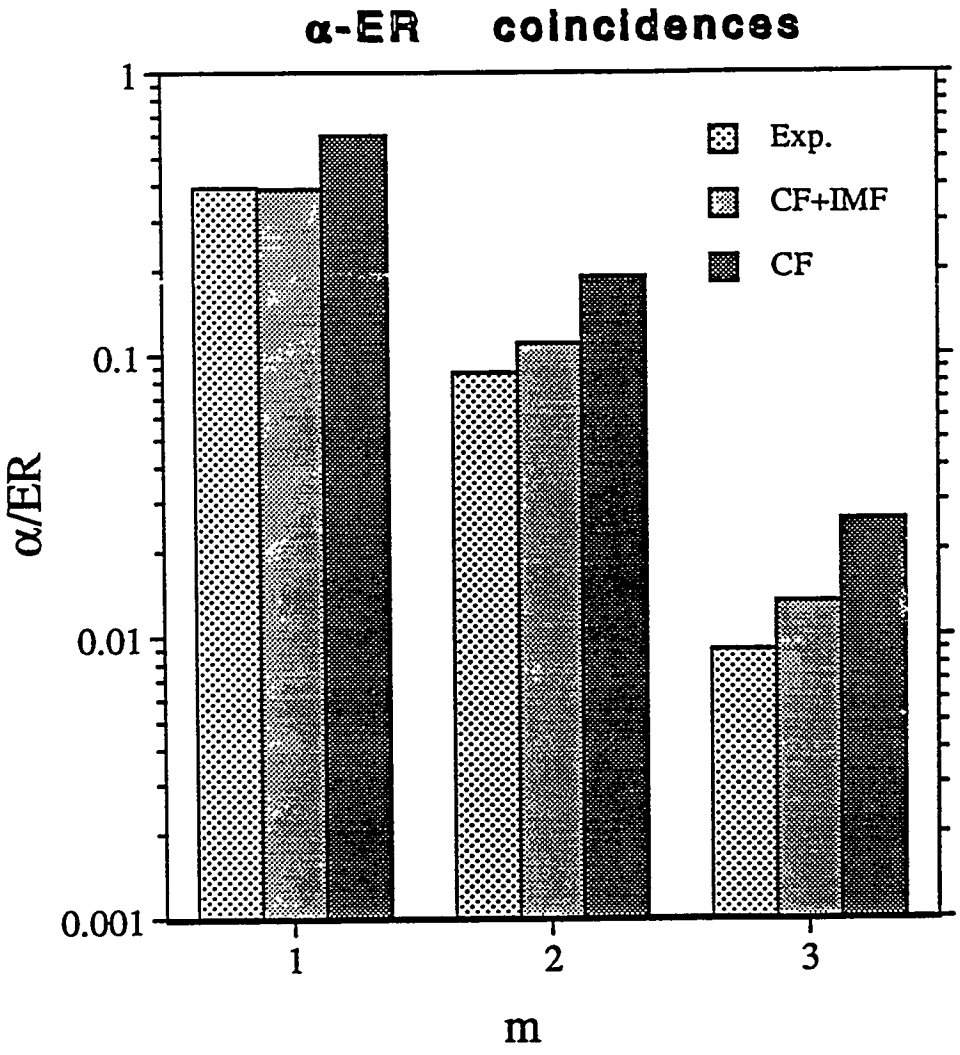

Fig 10

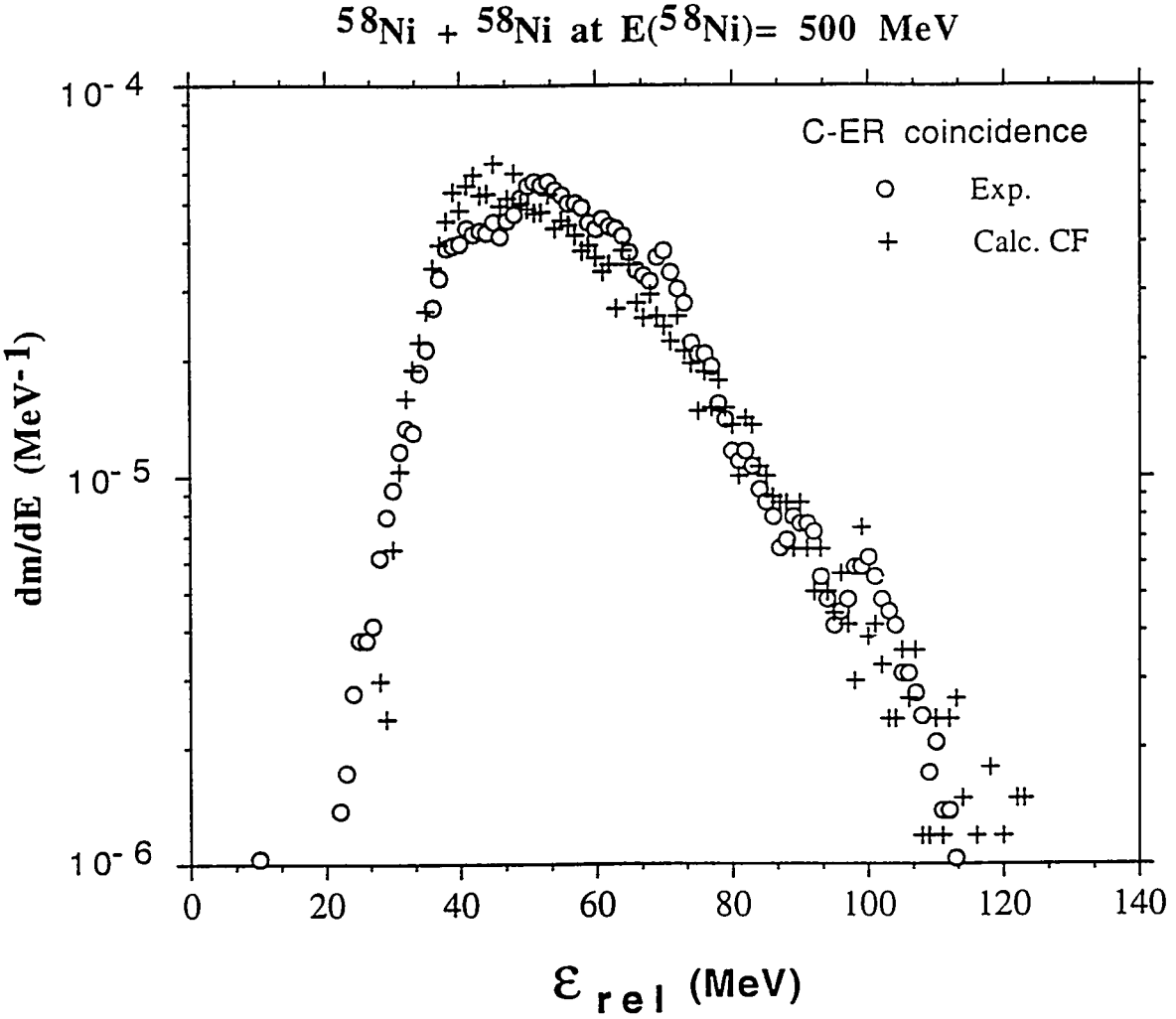
^{58}Ni + ^{58}Ni at E(^{58}Ni)= 500 MeV
C-ER coincidence
Exp.
Calc. CF
dm/dE (MeV^{-1})
10^{-4}
10^{-5}
10^{-6}
0
20
40
60
80
100
120
140
ε_{rel} (MeV)

Fig 4

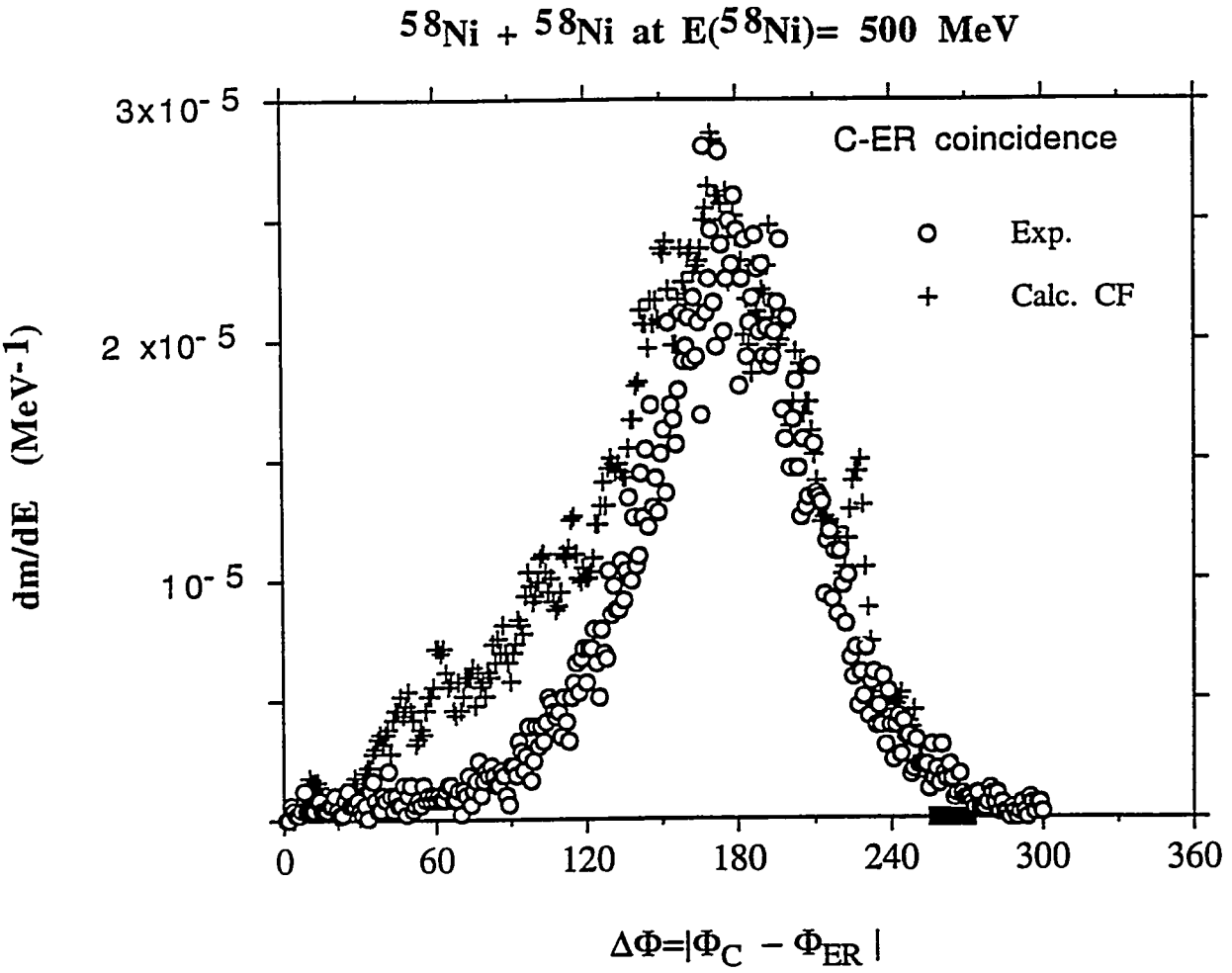
58Ni + 58Ni at E(58Ni)= 500 MeV
C-ER coincidence
Exp.
Calc. CF
dm/dE (MeV-1)
3x10-5
2 x10-5
10-5
0
60
120
180
240
300
360
ΔΦ=|ΦC − ΦER |

Fig 2

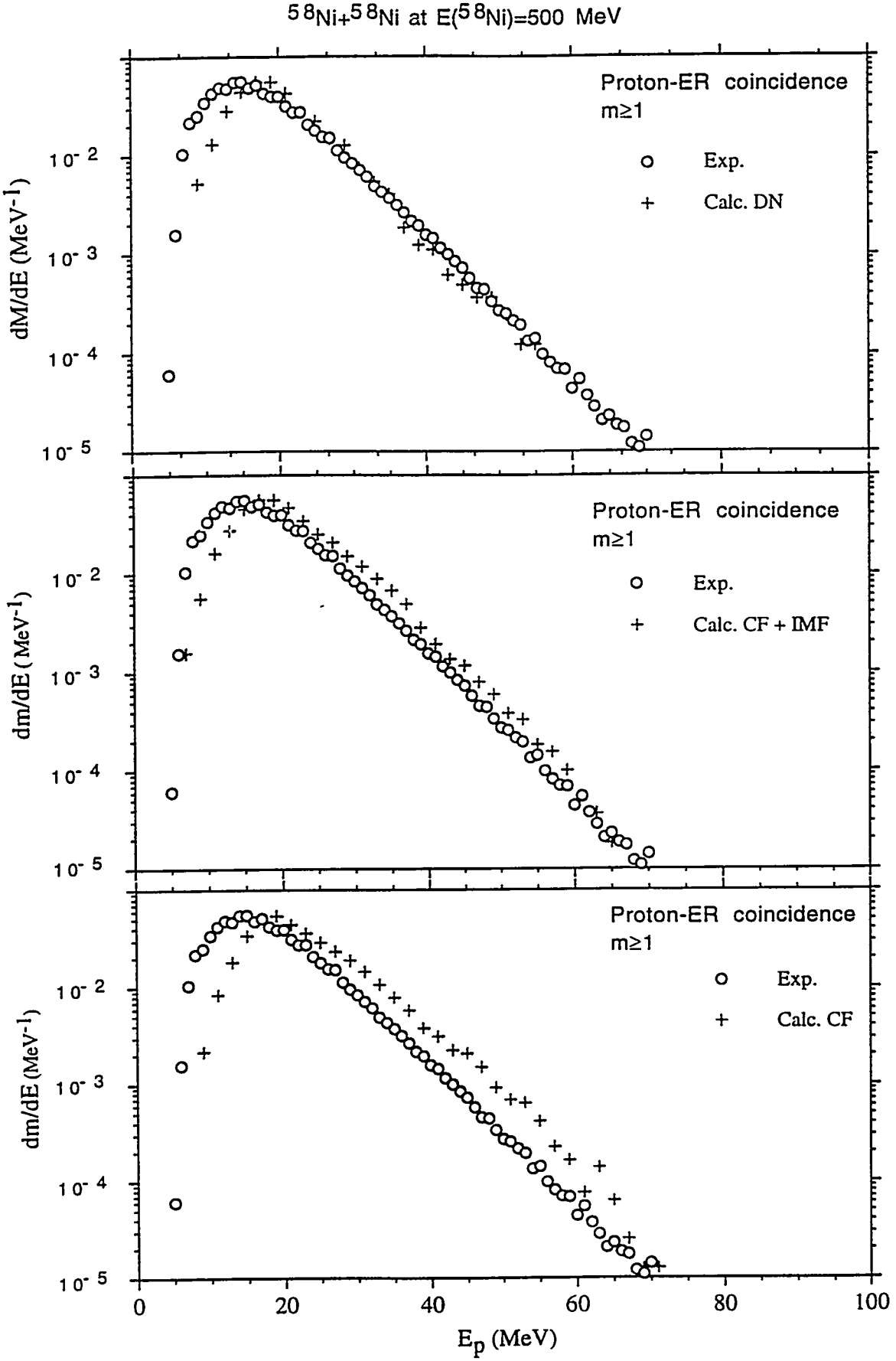
58Ni+58Ni at E(58Ni)=500 MeV
Proton-ER coincidence
m≥1
Exp.
Calc. DN
dM/dE (MeV-1)
Proton-ER coincidence
m≥1
Exp.
Calc. CF + IMF
dm/dE (MeV-1)
Proton-ER coincidence
m≥1
Exp.
Calc. CF
dm/dE (MeV-1)
10- 2
10- 3
10- 4
10- 5
0
20
40
60
80
100
Ep (MeV)

Fig 13

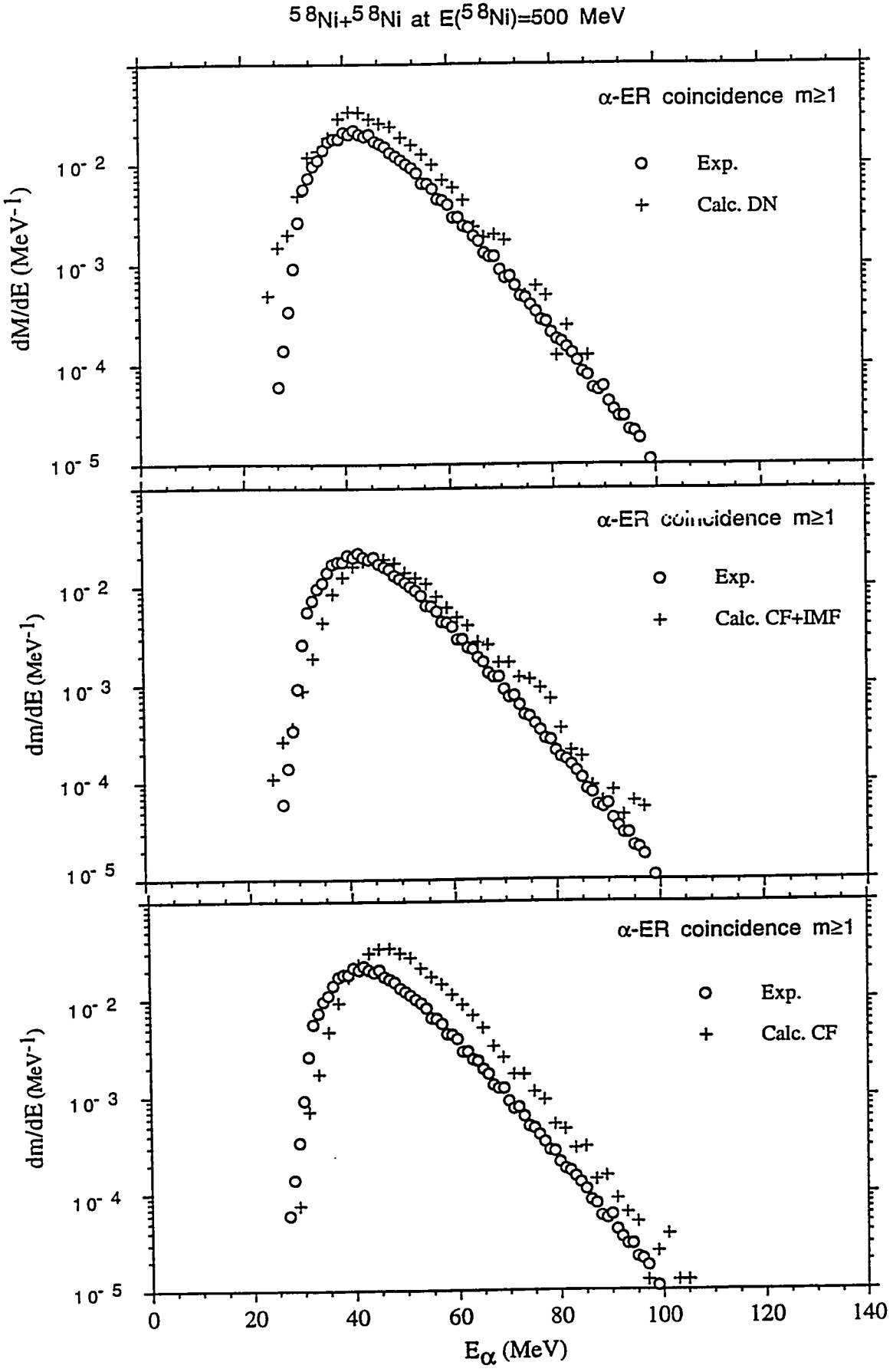
$^{58}Ni+^{58}Ni$ at E(^{58}Ni)=500 MeV
α-ER coincidence m≥1
Exp.
Calc. DN
dM/dE (MeV^{-1})
α-ER coincidence m≥1
Exp.
Calc. CF+IMF
dm/dE (MeV^{-1})
α-ER coincidence m≥1
Exp.
Calc. CF
dm/dE (MeV^{-1})
10^{-2}
10^{-3}
10^{-4}
10^{-5}
0
20
40
60
80
100
120
140
E_α (MeV)

Fig 14

DISCLAIMER